

A Multirange Vehicle Speed Prediction With Application to Model Predictive Control-Based Integrated Power and Thermal Management of Connected Hybrid Electric Vehicles

Qihao Hu

Department of Naval Architecture and Marine Engineering, University of Michigan, Ann Arbor, MI 48109
e-mail: qhhu@umich.edu

Mohammad Reza Amini

Department of Naval Architecture and Marine Engineering, University of Michigan, Ann Arbor, MI 48109
e-mail: mamini@umich.edu

Ashley Wiese

Ford Motor Company, Dearborn, MI 48124
e-mail: awiese@ford.com

Julia Buckland Seeds

Ford Motor Company, Dearborn, MI 48124
e-mail: jbuckland@ford.com

Ilya Kolmanovsky

Department of Aerospace Engineering, University of Michigan, Ann Arbor, MI 48109
e-mail: ilya@umich.edu

Jing Sun

Department of Naval Architecture and Marine Engineering, University of Michigan, Ann Arbor, MI 48109
e-mail: jingsun@umich.edu

Connectivity and automated driving technologies have opened up new research directions in the energy management of vehicles which exploit look-ahead preview and enhance the situational awareness. Despite this advancement, the vehicle speed preview that can be obtained from vehicle-to-vehicle/infrastructure (V2V/I) communications is often limited to a relatively short time-horizon. The vehicular energy systems, specifically those of the electrified vehicles, consist of multiple interacting power and thermal subsystems that respond over different time-scales. Consequently, their optimal energy management can greatly benefit from long-term speed prediction beyond that available through V2V/I communications. Accurately extending the look-ahead preview, on the other hand, is fundamentally challenging due to the dynamic nature of the traffic environment. To address this challenge, we propose a data-driven multirange vehicle speed prediction strategy for arterial corridors with signalized intersections, providing the vehicle speed preview for three different ranges, i.e., short-, medium-, and long-range. The short-range preview is obtained by V2V/I communications. The medium-range preview is realized using a neural network (NN), while the long-range preview is predicted based on a Bayesian network (BN). The predictions are updated in real-time based on the current state of traffic and incorporated into a multihorizon model predictive control (MH-MPC) for integrated power and thermal management (iPTM) of connected vehicles. The results of design and evaluation of the performance of the proposed data-informed MH-MPC for iPTM of connected hybrid electric vehicles (HEVs) using traffic data for real-world city driving are reported. [DOI: 10.1115/1.4052819]

Keywords: power and thermal management, model predictive control, multitime-scale optimization

1 Introduction

Connected and automated vehicles (CAVs) can exploit the look-ahead preview of vehicle speed and enhance situational awareness to improve energy efficiency, particularly for electrified vehicles including hybrid electric vehicles (HEVs), plug-in HEVs, and electric vehicles. While many studies have highlighted the energy saving potential using vehicle speed preview information, the current approaches can accurately forecast vehicle speed over a relatively short horizon [1,2]. At the same time, since the power and thermal subsystems of CAVs have very different time constants, it is beneficial for the integrated power and thermal management (iPTM) to leverage both short- and long-range vehicle speed prediction [3–5]. In Ref. [5], the simulation results showed a 2–5% increase in energy savings by exploring longer-range preview when compared to a conventional strategy with only short-range preview. Unfortunately, accurate long-range vehicle speed forecasting is fundamentally challenging, particularly for city driving scenarios with more uncertain traffic conditions.

Existing vehicle speed prediction methods can be divided into model-based and data-driven methods [6,7]. Model-based vehicle speed prediction methods rely on predefined parametric models

reflecting driver behavior. One example of this approach was the car-following model proposed by Jing et al. [8]. The result showed that the proposed algorithm can accurately predict the vehicle speed over a short horizon (e.g., 5 s) under low CAV penetration rates. In Ref. [9], the vehicle speed over a 3-s horizon was estimated using random forest regressor when the vehicle approaches signalized intersections. Overall, such parametric models are often applicable for short-term vehicle speed prediction under deterministic driving scenarios.

Data-driven methods for vehicle speed prediction have also been considered, including nonparametric regressions [10], neural networks (NNs) [11–13], and support vector machines [14,15]. The focus in much of these works has been on vehicle speed prediction over a short horizon, and only limited studies have been pursued to address long-range speed forecasts. In particular, Park et al. [16] first developed an NN for vehicle speed prediction at traffic sensor locations along a given route, demonstrating that the proposed NN provides an accurate speed prediction over a horizon of 30 s. Next, based on the speed prediction and the distance between adjacent sensors, the traveling time and average vehicle speed between sensors were calculated. Finally, the long-range vehicle speed profile was predicted by combining the average speed of every segment. In Ref. [17], a two-level vehicle speed prediction framework was developed. At the first level, the average vehicle speed of traffic flow was estimated based on an NN. At the second level, a hidden Markov model was utilized for

Contributed by the Dynamic Systems Division of ASME for publication in the JOURNAL OF DYNAMIC SYSTEMS, MEASUREMENT, AND CONTROL. Manuscript received April 29, 2021; final manuscript received September 22, 2021; published online November 22, 2021. Assoc. Editor: Mahdi Shahbahkhti.

individual vehicles. While Refs. [16] and [17] aimed at extending the vehicle speed prediction horizon, they only focused on predicting the average speed over road segments, and the traffic events (e.g., stops) within the segments were not captured.

To address the aforementioned problem, in Ref. [18], an urban driving route was considered and decomposed into segments of four types, i.e., free flow, stop sign, traffic light, and turn. For each segment type, an NN was trained for vehicle speed prediction. It was shown that the proposed approach can outperform two baseline methods based on the speed limit and traffic pattern over urban routes. While the study in Ref. [18] showed an improvement in vehicle speed prediction in terms of the mean absolute error, the prediction performance for traffic events (e.g., stops, acceleration/brake at intersections) was not investigated. Moreover, the traffic signal information was not available, and the NN was trained regardless of the signal status, which may lead to large errors in speed prediction of a vehicle arriving/departing intersections. Overall, vehicle speed prediction in arterial corridors with multiple intersections and over relatively long horizons has not been sufficiently studied.

In this paper, a multirange vehicle speed prediction approach for urban driving scenarios is proposed. This approach leverages both historical and real-time vehicle-to-vehicle/infrastructure (V2V/I) communications data to predict vehicle speed over multiple horizons with different levels of fidelity. For the short-range horizon, e.g., 5–10 s, the vehicle speed prediction obtained through V2V/I communications is assumed of high accuracy. For the long-range horizon (until the end of the trip), a Bayesian network (BN) is developed to estimate the most probable driving scenario and provide the corresponding speed trajectory. In the process, the passing/stopping events at all intersections, average cruise speed between intersections, and the end time of the trip are estimated. Furthermore, to mitigate the uncertainty of long-range prediction, this paper explores a medium-range speed prediction, where the accuracy lies between that of the short- and long-range preview. This medium-range preview is designed to predict the passing/stopping event at the next intersection using an NN. Additionally, based on V2V communication, the stop time, departure time, and queue length are estimated.

To demonstrate the benefits of the proposed multirange vehicle speed prediction framework in enhancing the energy efficiency of CAVs, we integrate it with an optimization-based energy management strategy for iPTM of power-split HEVs. The objective of iPTM is to minimize fuel consumption while enforcing the power and thermal constraints over the trip. The wintertime condition is considered in this study with cold ambient temperature and constant cabin heating demands. A model predictive control (MPC) is applied to implement iPTM given its ability to handle state/input constraints and optimize a cost function reflective of fuel/energy consumption [19–23]. The performance of the controller with different speed predictions is assessed in order to quantify the impact on energy consumption.

The contributions of this paper include (i) the development of a multirange vehicle speed prediction framework for urban driving, and (ii) the incorporation of the multirange vehicle speed prediction into a multihorizon MPC for iPTM of power-split HEVs and demonstration of the associated fuel savings using real-world driving scenarios.

The rest of the paper is organized as follows: Sec. 2 introduces our data-driven multirange vehicle speed prediction strategies, including the long-range speed prediction based on BN and the medium-range prediction based on NN. Section 3 introduces the physics-based and control-oriented models representing the power and thermal loops of the HEVs system. Next, the MPC algorithm developed for minimizing the fuel consumption of HEVs is described in Sec. 4. Section 5 reports the simulation results of iPTM which incorporates the proposed speed prediction strategy. Finally, the conclusion and future work are summarized in Sec. 6.

2 Data-Driven Multirange Vehicle Speed Prediction

In this section, a multirange vehicle speed prediction framework is introduced for urban driving cycles which enables

efficient iPTM of CAVs. We assume that all the intersections in the driving route are signalized and that the destination is known from the beginning of the trip. As shown in Fig. 1, the vehicle speed preview is divided into three ranges as follows:

- *Short-range preview*: For the short-range, e.g., 5–10 s ahead, the vehicle speed prediction could be obtained by exploiting V2V/I communications available to connected HEVs.
- *Long-range preview*: The long-range preview covers the entire trip, for which the most probable driving scenario is predicted. Additionally, the passing/stopping at all remaining intersections, the cruise speed between intersections, and the end time of the trip are predicted according to the predicted driving scenario.
- *Medium-range preview*: In order to mitigate the uncertainty of long-range speed prediction, this paper also explores a medium-range preview. This medium-range preview addresses the portion of the trip from the current vehicle location to the next intersection and involves prediction for passing/stopping event, arrival/stop time, and departure time at the next intersection.

Our approach to implement the proposed multirange vehicle speed prediction is data-driven. The dataset and the prediction algorithms are detailed in what follows.

2.1 Real-World Traffic Simulation Data. As a representative case study, a traffic simulation model of a city corridor built in the microscopic traffic simulation software VISSIM [24,25] is adopted. The city corridor is located on Plymouth Road, in Ann Arbor, MI with six intersections. This corridor is one of the busiest commuting routes connecting the downtown of Ann Arbor to the U.S.-23 highway. Its total length is around 2.2 mi, and it has two lanes in each direction. Moreover, in this case study, all the intersections in the Plymouth Road corridor are signalized, and the distance between intersections is within 1000 m.

The VISSIM traffic simulation model has been calibrated with real-world data collected during the afternoon rush hour (4:00–5:00 p.m.). The collected data obtained from infrastructure-based sensors include traffic volume and turning ratio at each intersection, see Refs. [25] and [26] for details on calibration and validation of the VISSIM model. Since the actual signal timing policy implemented over the Plymouth Road is unknown and is considered proprietary to the city of Ann Arbor, a coordinated fixed-time signal timing policy with a cycle length of 150 s was applied to all six intersections. The VISSIM model was used to generate the vehicle trajectory data.

The VISSIM model was run for two and a half hours, while the parameters of the traffic model were kept fixed and the traffic congestion-level did not change during the simulation. The congestion-level was set to medium (roughly 900 vehicles per hour, which may vary from one intersection to another). This congestion-level represents undersaturated traffic, in which the queues at signalized intersections can be fully discharged during the traffic signal green interval. The embedded driver model used in VISSIM is kept fixed for all the simulated vehicles, meaning the key parameters associated with a driver's behavior (e.g., rate of change in speed, maximum speed) are the same.

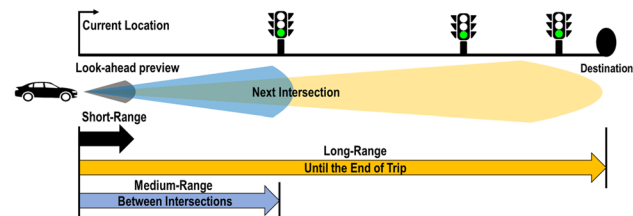


Fig. 1 The concept of multirange vehicle speed previews

During the simulation period, the time-series speed data of each simulated vehicle were collected and stored. Next, among all the stored vehicles' speed data, the speed profiles of 1478 vehicles driving through the entire corridor in the same direction (i.e., entering from the west and exiting from the east side) were identified and used for our case study. Data of other vehicles that either exited the corridor before reaching the destination or entered the corridor in between were not included. For the remainder of the paper, we refer to these vehicle speed data generated by the VISSIM model as the traffic data. Note that all the vehicles in the simulation model are of the same type, i.e., small size passenger vehicles.

2.2 Short-Range Preview. In this study, an accurate vehicle speed prediction over a relatively short-range horizon, e.g., 5–10 s, is assumed to be available and known. A sufficiently accurate short-range speed prediction can be informed by V2V/I communications through model-based [25], stochastic [20,27], data-driven [28,29], and learning-based [30] methods.

Remark 1. It should be noted that, in actual traffic, short-range speed predictions are subject to uncertainties, e.g., unexpected events such as vehicle cut-in that could lead to speed prediction errors. This study, however, is focused on enhancing the speed prediction accuracy over long and medium horizons.

2.3 Long-Range Preview. We first present the long-range speed prediction strategy and motivate the need for a medium-range speed prediction, which will be presented in Sec. 2.4. The long-range vehicle speed prediction becomes necessary given relatively slow thermal dynamics. As shown in Fig. 1, the long-range vehicle speed preview defined in this work covers the segment from the end of the short-range preview until the end of the trip. Accurately predicting vehicle speed over such a long-range is fundamentally challenging. Figure 2 shows the mean value and standard deviation of all 1478 vehicle speed trajectories collected over the Plymouth Road as described in Sec. 2.1. It can be seen that this aggregated average speed, with large standard deviation, does not provide insightful information about the traffic flow. For example, the stop-and-go behavior at the signalized intersections cannot be predicted, making the aggregated average speed not meaningful for long-range vehicle speed prediction. The aforementioned observations of the aggregated vehicle speed suggest that additional data processing is needed to get clearer patterns of the long-range preview and reduce the error of forecast.

To enable long-term vehicle speed prediction, a BN is adopted to classify the traffic data and generate a long-term driving scenario tree. Specifically, we treat passing/stopping events at intersections as stochastic variables (x) dependent on the observed events at upstream intersections. These events influence the probability distributions of the variables at downstream intersections. A BN can take into account the causal relationship between the variables of interest and represent conditional dependencies between a set of random variables [31]. The BN can be exploited to generate a dynamic scenario tree to obtain the joint probability

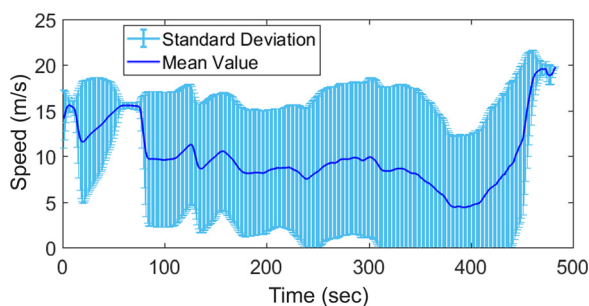


Fig. 2 The mean value and standard deviation of all simulated vehicle speed data collected over the Plymouth Road corridor

distribution of passing/stopping events at different intersections, from which the “most probable” driving scenario is determined. The concept of this BN for urban driving is presented in Fig. 3, in which the most probable driving scenario is updated in real-time after the vehicle passes each intersection according to (i) observations obtained from the actual driving, and (ii) changes in the probability distribution of passing/stopping events as the traffic evolves. As an example and according to Fig. 3, while from the beginning the vehicle is predicted to pass the first intersection (Fig. 3(a)) as the computed probability of passing is larger than that of stopping, the actual observation indicates that the vehicle stops at the first intersection. Consequently, the most probable driving scenario is updated once the vehicle departs the first intersection (Fig. 3(b)).

For the BN that is developed for an arterial corridor, we interpret an arc from intersection k to $k + 1$ as stop/pass at intersection k followed by stop/pass at intersection $k + 1$. For a corridor with H intersections, each intersection is considered as a node represented by x_k ($k = 1, \dots, p, \dots, H$), where x_k takes the values of “true” for passing and “false” for stopping. At intersection p , the joint probability distribution for the remaining trip is updated as

$$\Pr(x_p, \dots, x_H) = \prod_{k=p}^H \Pr(x_k | x_{p:k}) \quad (1)$$

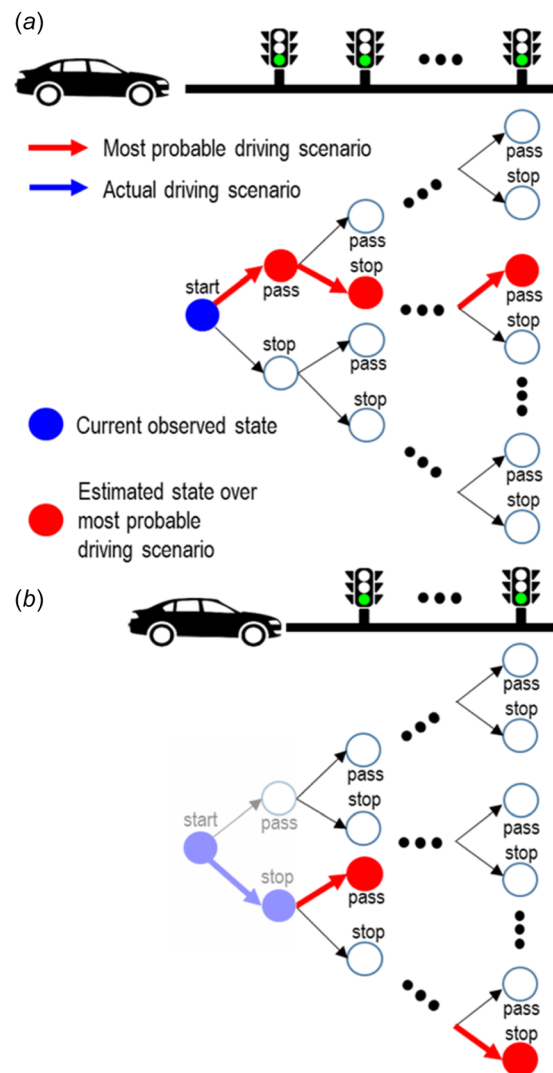


Fig. 3 Driving scenario generation for estimation of most probable driving scenario over an arterial corridor using BN

Here, $\Pr(x_k|x_{P_k})$ is the conditional probability distribution associated with intersection k , and P_k is the set of indices labeling the upstream intersections of the k th intersection [31,32]. For instance, $\Pr(x_4|x_1 = \text{True}, x_2 = \text{False}, x_3 = \text{False})$ indicates the probability of the ego-vehicle passing the fourth intersection after it has passed the first, but stopped at the second and at the third intersections. Note that the directed arc of the BN should flow forward both in the time direction and in the traffic flow direction [31].

The conditional probability distribution of the passing/stopping events at intersections is inferred from the traffic data according to Eq. (1). Note that, while in this paper the dataset is built based upon the VISSIM traffic simulation model, in practice, the connected vehicles' speed data can be collected, analyzed, and updated by a central/cloud server in real-time, constructing the historical traffic dataset for a specific memory length. The speed of a vehicle traveling through the corridor is estimated using the branch with the highest product of probabilities, which represents the most probable driving scenario until the end of the trip. The branch selection is updated during the trip based on the observed states (i.e., observation of actual passing/stopping events at given intersections).

The vehicle data collected over the Plymouth Road driving corridor are used to inform the proposed BN. The results are presented in Fig. 4. It can be seen that the BN for the section of Plymouth Road consists of ten main branches. Note that there are three minor branches with a probability of less than 0.01 that are excluded from the BN. The time-varying mean and standard deviation of the vehicle speed for each of the ten branches of the BN are reported in Fig. 5. It can be observed that the prediction of vehicle speed over a given branch provides a marked improvement over using the average speed of all trajectories. Therefore, this BN will be leveraged for long-range vehicle speed prediction. Additionally, the BN can be used to predict passing/stopping events at signalized intersections and the end time of the trip that are useful in energy management optimization.

To summarize, a BN is developed to provide the conditional probabilities of passing/stopping events at signalized intersections. When used in real-time for vehicle speed prediction, the

vehicle speed profile prediction corresponds to the branch with the highest probability. The probability for each branch is updated each time a stop/pass event is observed. The developed BN is designed to capture an "average" behavior of drivers based on the data described in Sec. 2.1. In actual traffic, drivers have different levels of aggressiveness, requiring the adaptation of the long-term speed prediction for each "ego" vehicle. For automated vehicles, the sensitivity of the long-term speed predictions to these types of individual vehicles' behaviors is expected to be smaller. The developed BN treats vehicles with noticeably different behaviors, as compared to the average traffic, as outliers that have less impact on the average traffic flow dynamics.

Remark 2. Expanding the proposed BN-based approach to corridors with more intersections requires a more systematic way to generate a scalable driving scenario tree. To that end, insights from scenario tree generation in stochastic MPC [20,33] may be considered.

2.4 Medium-Range Preview. In Sec. 2.3, a BN is developed to provide a long-range vehicle speed forecast by predicting the most probable driving scenario. However, sometimes, the prediction error of forecast passing/stopping events at intersections can be large. For example, as shown in Fig. 4, for the vehicles passing through the first intersection, the probabilities of passing and stopping at the second intersection are 51.7% and 48.3%, respectively. Thus, almost half of the vehicles (passing the first intersection) are expected to be mispredicted using the BN, and this introduces substantial uncertainty into the long-range vehicle speed prediction due to significant differences between the average speed of the branches. Another limitation of this long-range vehicle speed prediction is the uncertainty around the stop time and departure time at intersections. As shown in Fig. 6, branch 3 displays large variations in the stop times and departure times at intersections. This variation may be attributed to the queuing dynamics and traffic signal phase switch. Additionally, most of the vehicles have similar acceleration/deceleration profiles but shifted in time which confounds the average speed. To address these issues, a medium-range preview is introduced.

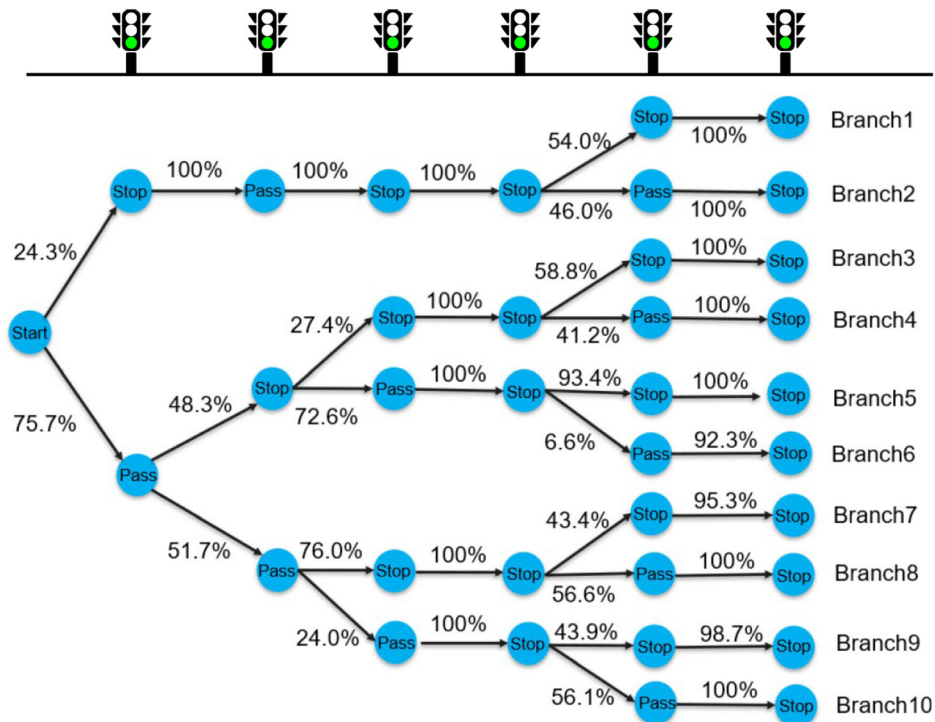


Fig. 4 The BN developed based on the historical data over an arterial corridor. The numbers over the arrows indicate probability.

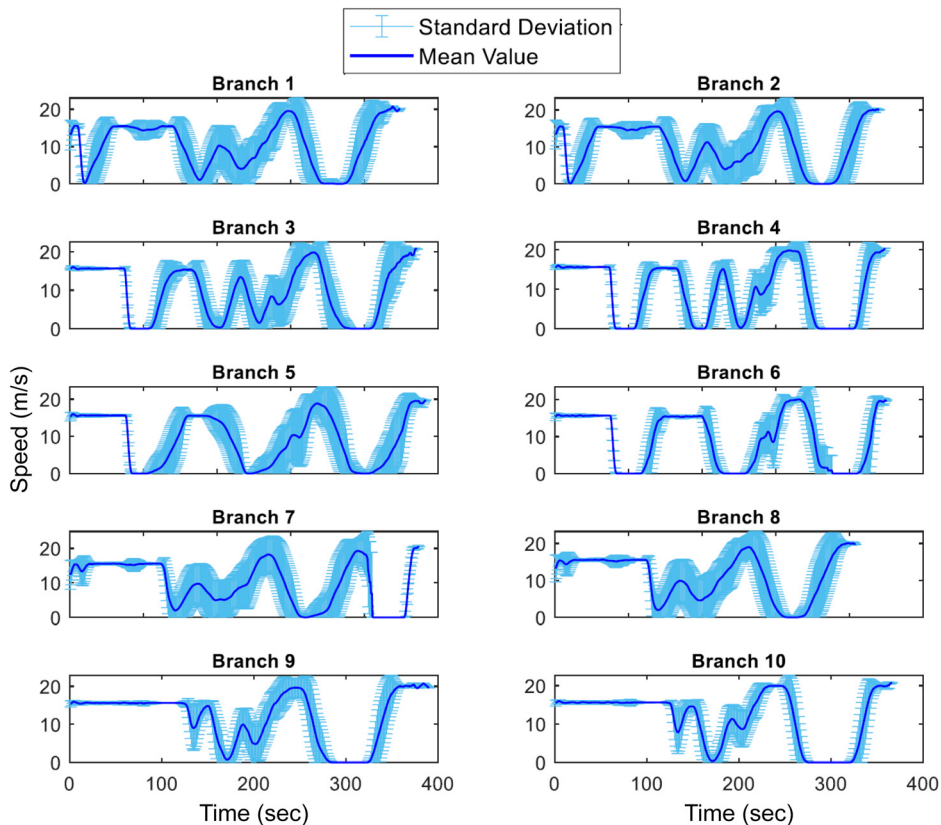


Fig. 5 The mean value and standard deviation of vehicles in ten branches classified by BN

Assuming an urban driving scenario with signalized intersections, the medium-range preview involves the prediction of vehicle speed from the end of the short-range preview to the next intersection. Figure 7 illustrates the models of vehicle speed trajectories assumed in the medium-range that are dependent on the forecasted passing/stopping events at the next intersection. The vehicle speed between intersections is assumed to be equal to the average cruise speed (V_{cruise}). Note that the cruising here means that the vehicles travel at the speed limit of the segments (in VISIM, the cruising speed between intersections is set to the speed limit of the corresponding segment) and varies within a range of 2 m/s. For vehicles stopping at the next intersection, we define the stop time (T_{stop}) and stop duration (T_{dura}) as shown in Fig. 7. For vehicles passing through the next intersection, the arrival time ($T_{arrival}$) is defined as the time to reach the stop bar at the next intersection, see Fig. 7, and is estimated as

$$T_{arrival} = \frac{s_{bar}}{V_{cruise}} \quad (2)$$

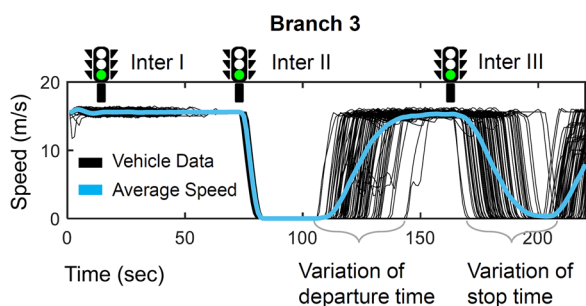


Fig. 6 The variation of the stop time and departure time at intersections for the vehicle data in branch 3

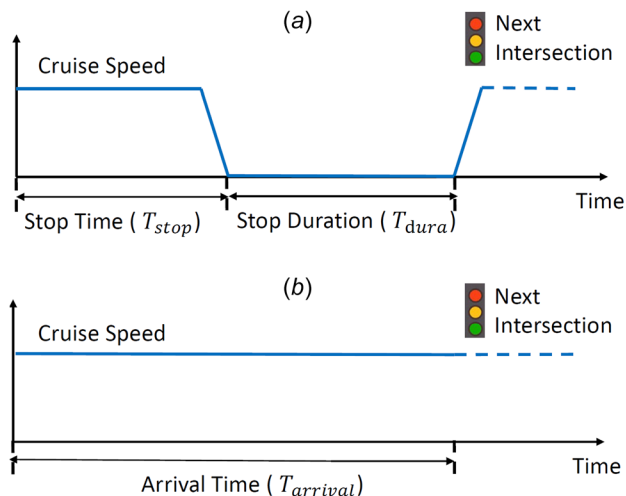


Fig. 7 Predicted vehicle speed in the medium-range for ego-vehicles (a) stopped at next intersection and (b) passing through the next intersection

where s_{bar} is the distance between the vehicle and the stop bar at the next intersection. Note that it is assumed that the location of the vehicle and the stop bar of intersections are available during the trip, and thus s_{bar} can be calculated in real-time. As shown in Fig. 8, for vehicles stopping at the next intersection, both T_{stop} and T_{dura} are significantly influenced by the queue length (s_{queue}) and thus are predicted as follows:

$$T_{stop} = \frac{s_{bar} - s_{queue}}{V_{cruise}} \quad (3)$$

$$T_{dura} = T_{signal} + T_{queue} \quad (4)$$

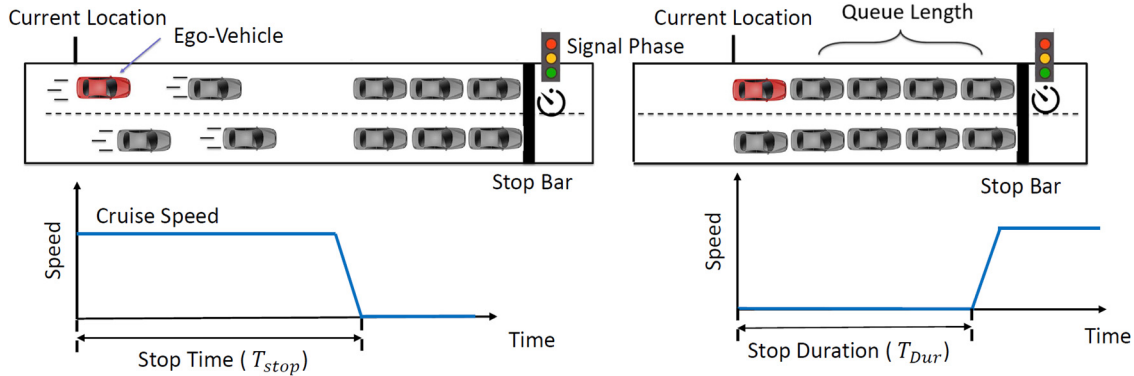


Fig. 8 The concept of vehicle speed in the medium-range preview

where T_{signal} and T_{queue} are the time duration that an ego-vehicle needs to wait for (i) the traffic signal phase switch and (ii) the discharge of the queue, respectively. It can be seen that, in order to predict the vehicle speed using the aforementioned models, pass/stop and queue length information for the next intersection are needed.

To this end, a real-time vehicle speed prediction is proposed, based on V2V/I communication and passing/stopping prediction over the medium-range. Figure 9 presents the flowchart of the proposed strategy. Once an ego-vehicle enters a segment between two intersections, the model of the vehicle speed trajectory in Fig. 7 is selected based on the predicted passing/stopping event at the next intersection. If this vehicle is predicted to pass through the intersection, the arrival time is calculated by Eq. (2), and the vehicle speed trajectory in the medium-range is predicted using the model in Fig. 7(b). If this vehicle is predicted to stop, T_{stop} , T_{dura} , as well as s_{queue} need to be predicted. To accomplish this, first, we assume the number of vehicles (N) ahead of this ego-vehicle in the respective road segment is known. Note that, in a road segment between two intersections, if coordinates of the vehicles in front are known either through the vehicle-to-vehicle communications [34], through the individual vehicle-to-

infrastructure (cloud) communications, or through infrastructure-based sensing, the number of vehicles in front of an ego-vehicle (N) can be inferred. Approaches that are based on vision-based systems onboard of the ego-vehicle can also be used.

In the next step, the passing/stopping events for all these N vehicles are predicted, and as a result, K vehicles are predicted to stop and the remaining $N - K$ vehicles pass. With K being the number of vehicles in the queue, s_{queue} can be estimated assuming that every vehicle adds a fixed length to the queue. Additionally, the dependence of s_{queue} on T_{queue} based on Plymouth Road vehicle data is shown in Fig. 10. It can be observed that the relationship can be reasonably represented by a second-order polynomial, $T_{\text{queue}} = as_{\text{queue}}^2 + bs_{\text{queue}} + c$. Then, T_{stop} and T_{dura} are calculated using Eqs. (3) and (4), and the vehicle speed trajectory is predicted using the model in Fig. 7(a).

Remark 3. Depending on the method used to estimate the number of vehicles in front of an ego-vehicle (N), communication gaps between vehicles could occur, leading to uncertainty in estimating N . While it is outside the scope of this paper, the impact of such uncertainties and the nonhomogeneous behavior of the vehicles are topics that warrant future investigations.

To implement the above approach, the prediction of the passing/stopping event is required. The algorithm shown in Fig. 9 is generic and is not restricted to a particular model to predict the passing/stopping event. In this paper, a NN-based solution is used for this purpose. In this paper, we propose a decentralized NN design process, in which one NN is trained for each road segment between two adjacent intersections. An alternative approach to this strategy is to develop one single centralized NN covering all the road segments. The main reason for adopting a distributed NN in this paper is because it greatly helps to keep the NN structure and its training process simple and computationally fast.

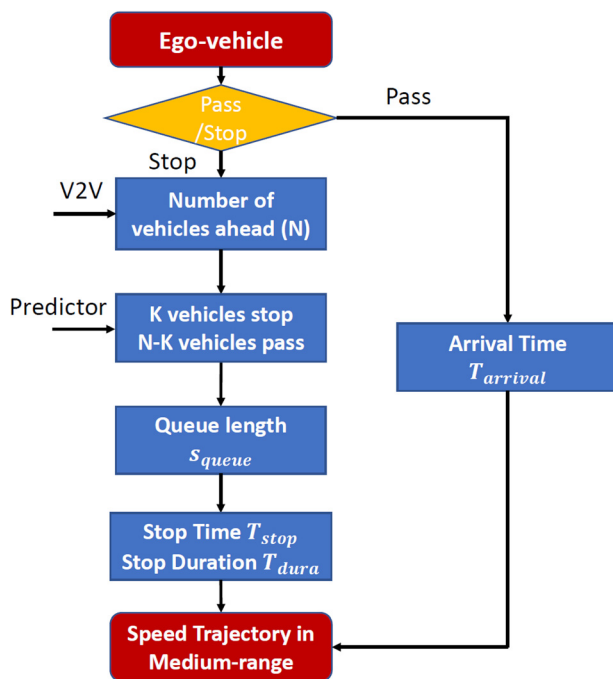


Fig. 9 The flowchart to generate the vehicle speed trajectory in medium-range

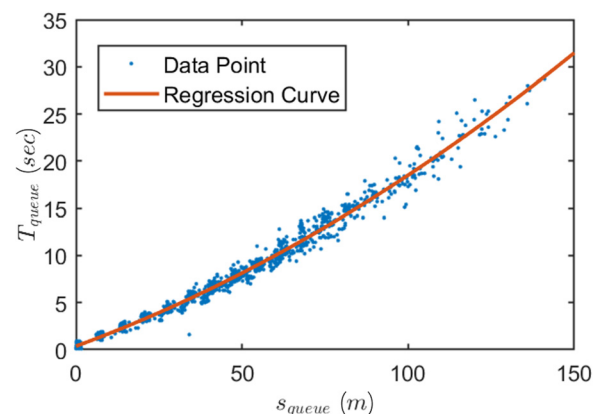


Fig. 10 The relationship between queue length (s_{queue}) and the discharge time of queue (T_{queue})

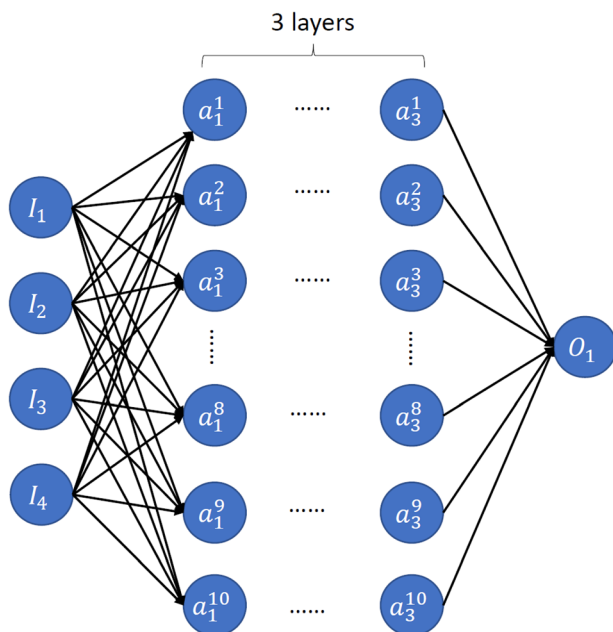


Fig. 11 The structure of NN designed in medium-range preview

Moreover, since the ratio of the vehicles that may enter/exit at an intersection and the traffic flow and the length of one segment could be different than other segments, different NNs for different segments may be needed to represent traffic patterns more accurately to inform the medium-range speed forecast.

The proposed NN, shown in Fig. 11, has four inputs, i.e., the current vehicle speed, trip distance (to the start point of the route), trip time in the route, and current signal timing and phase of the next intersection, and one output, i.e., passing/stopping at the next intersection. Note that it is assumed that the current signal phase of intersections is available by V2I communications. The NN is a feedforward network and consists of three hidden layers with ten neurons each (a in Fig. 11). The logistic sigmoid function is used as the activation function. The NN is developed using MATLAB DEEP LEARNING TOOLBOX for pattern recognition. The weight and bias values of the NN are trained with the scaled conjugate gradient method. Twenty percent of the Plymouth Road simulation data is used to train the NN, as using a higher percentage of training data did not improve the predictions. The remaining 80% of the data is used to assess prediction accuracy, which is summarized in Table 1. For each intersection, one NN with the aforementioned structure is trained independently of others. Note that because all the vehicles in the dataset stop at intersection IV, the accuracy of NN prediction is 100%. As compared with the BN, NN provides a better accuracy (higher than 90% for all intersections) in predicting passing/stopping events at the next intersection which inform a more accurate vehicle speed forecast over a medium-range.

Remark 4. The proposed long-range speed prediction approach based on the BN's branch with the highest probability is computationally very fast and can be updated in real-time. However, there might be branches with slightly smaller probabilities that will not be picked up as the long-term preview by the BN. The integration of the medium-range preview could compensate for such

Table 1 The accuracy of NN in predicting passing/stopping events at six intersections

Intersection number	I	II	III	IV	V	VI
Accuracy (%)	97.3	99.4	94.9	100.0	94.8	99.1

scenarios. For example, if based on the most probable driving scenario, a vehicle is predicted to “pass” an upcoming intersection, but the medium-range predictor estimates it to “stop,” then in the final speed preview, the stop event is implemented as the more reliable prediction.

3 Hybrid Electric Vehicle Power and Thermal Models

We now consider the integration of our proposed multirange vehicle speed prediction approach into a model predictive control for energy management of a power-split HEV, operating at cold ambient temperature in wintertime. The power and thermal models adopted in this study were developed and validated in Ref. [35]. They are briefly reviewed in this section for completeness.

3.1 Battery Power-Balance Model. For a power-split HEV, the battery power ($P_{\text{bat}}^{\text{trac}}$) and the internal combustion engine power (P_{eng}) are blended to meet the traction power demand (P_{trac})

$$P_{\text{trac}} = P_{\text{bat}}^{\text{trac}} + P_{\text{eng}} \quad (5)$$

$$P_{\text{bat}} = P_{\text{bat}}^{\text{trac}} + P_{\text{bat}}^{\text{aux}} \quad (6)$$

The battery, in addition to assisting the engine in driving, also provides the auxiliary power ($P_{\text{bat}}^{\text{aux}}$) to the engine and cabin heating actuators (e.g., radiator fan, engine coolant pump, and heating, ventilation, and air conditioning blower). Note that in Eq. (6), P_{bat} is the total power provided by the battery.

The battery dynamics are represented by

$$\dot{\text{SOC}}(t) = f_{\text{SOC}}(t) = \frac{U_{\text{oc}} - \sqrt{U_{\text{oc}}^2 - 4R_{\text{int}}P_{\text{bat}}}}{2R_{\text{int}}C_{\text{bat}}} \quad (7)$$

where U_{oc} , R_{int} , and C_{bat} are the open-circuit voltage, internal resistance, and capacity of the battery, respectively.

3.2 Engine Coolant Temperature Model. Engine coolant temperature (T_{cl}) dynamics are modeled based on an energy balance equation [36]

$$\dot{T}_{\text{cl}}(t) = f_{T_{\text{cl}}}(t) = \frac{1}{M_{\text{eng}}C_{\text{eng}}} \left(\dot{Q}_{\text{fuel}} - P_{\text{eng}} - \dot{Q}_{\text{exh}} - \dot{Q}_{\text{air}} - \dot{Q}_{\text{heat}} \right) \quad (8)$$

where C_{eng} and M_{eng} are the equivalent thermal capacity and mass of the engine cooling system, respectively. Additionally, \dot{Q}_{fuel} , \dot{Q}_{exh} , \dot{Q}_{air} , and \dot{Q}_{heat} represent the heat rates released from the fuel combustion, exchanged through exhaust gases, dissipated by air convection, and delivered for cabin heating, respectively. In particular, \dot{Q}_{fuel} is a function of the fuel consumption rate (\dot{m}_{fuel}) and lower heating value (LHV) of the fuel

$$\dot{Q}_{\text{fuel}} = \text{LHV} \cdot \dot{m}_{\text{fuel}} \quad (9)$$

where \dot{m}_{fuel} is a function of engine speed (ω_e), torque (τ_e), and T_{cl}

$$\dot{m}_{\text{fuel}}(\omega_e, \tau_e, T_{\text{cl}}) = \alpha(T_{\text{cl}}) \cdot \dot{m}_{\text{fuel,nom}}(\omega_e, \tau_e) \quad (10)$$

and where $\dot{m}_{\text{fuel,nom}}(\omega_e, \tau_e)$ is the nominal fuel consumption rate calculated based on brake-specific fuel consumption map at fully warm conditions, while $\alpha(T_{\text{cl}})$ is a multiplier reflecting the sensitivity of fuel efficiency to the coolant temperature. These functions have been extracted from the AUTONOMIE¹ software for a power-split HEV [35]. In particular, when T_{cl} is higher than 60

¹AUTONOMIE is a MATLAB/SIMULINK-based system simulation tool for vehicle energy consumption and performance analysis developed by Argonne National Laboratory [37].

$^{\circ}\text{C}$, $\alpha = 1$, and when T_{cl} is less than 60°C , α increases, reflecting the degradation of engine efficiency caused by low temperatures. Moreover, the experimental validation of the models in Eqs. (7) and (8) can be found in our previous works [26,35].

4 Model Predictive Control-Based Integrated Power and Thermal Management of Hybrid Electric Vehicles

The objective of iPTM is to minimize the fuel consumption while enforcing the battery state-of-charge (SOC) and T_{cl} constraints and meeting the traction and cabin heating demands [5,38]. In our previous work, a multihorizon MPC was developed to account for multitime-scale characteristics of power and thermal subsystems of HEVs [4,39]. The multihorizon model predictive control (MH-MPC) is based on the solution to the following discrete-time optimal control problem:

$$\begin{aligned} \min_{P_{bat}(t)} \quad & \sum_{i=t}^{t+N_r-1} \dot{m}_{fuel}(i) \Delta t_1 + \sum_{i=t+N_r}^{t_{end}} \dot{m}_{fuel}(i) \Delta t_2 \\ \text{subject to} \quad & \text{SOC}(i+1) = \text{SOC}(i) + \Delta t_j \cdot f_{\text{SOC}}(i), \quad j \in \{1, 2\} \\ & T_{cl}(i+1) = T_{cl}(i) + \Delta t_j \cdot f_{T_{cl}}(i), \quad j \in \{1, 2\} \\ & 0.4 \leq \text{SOC}(i) \leq 0.8 \\ & 40^{\circ}\text{C} \leq T_{cl}(i) \leq 90^{\circ}\text{C} \\ & 0.99 \times \text{SOC}(0) \leq \text{SOC}(t_{end}) \leq \text{SOC}(0) \times 1.01 \\ & T_{cl}(0) = T_{cl,init}, \quad \text{SOC}(0) = \text{SOC}_{init} \end{aligned} \quad (11)$$

where N_r is length of the short receding horizon, t_{end} is the end time of the trip, and Δt_1 , Δt_2 are sampling times over the short receding and long shrinking horizons, respectively. Note that $j \in \{1, 2\}$ and

$$j = \begin{cases} 1, & \text{if } i \leq t + N_r - 1 \\ 2, & \text{if } i \geq t + N_r \end{cases} \quad (12)$$

The MH-MPC cost function represents the cumulative fuel consumption over (i) the short receding horizon calculated based on accurate short-range vehicle speed preview, and (ii) over the entire remaining trip beyond the receding horizon calculated based on the medium-range and long-range vehicle speed prediction. Additionally, a terminal constraint is applied to enforce the battery charge sustainability condition (i.e., enforce the final SOC close to the initial SOC). In order to enhance the feasibility of solving the optimization problem, a deviation of $\pm 1\%$ from the initial SOC is allowed for the final SOC.

To reduce the computational footprint of the MH-MPC over the long shrinking horizon, $\Delta t_2 > \Delta t_1$ is used. The MH-MPC is solved every 1 s with $\Delta t_1 = 1$ s and $\Delta t_2 = 10$ s, and the first element of the computed control input is applied to the system. Then, the receding horizon is shifted by Δt_1 , and the shrinking horizon is shortened by Δt_1 . Note that when the remaining trip time is shorter than $\Delta t_1 N$, the multihorizon is no longer needed, and there is only one shrinking horizon remaining in the cost function with the sampling time of Δt_1 .

5 Results and Discussions

In order to assess the benefits of the proposed framework, the multirange vehicle speed prediction strategy is applied to enable the iPTM of MH-MPC. Three cases shown in Fig. 12 are considered over the long shrinking horizon as following:

Case A: The vehicle speed over the long shrinking horizon is assumed to be constant and equal to the current cruise speed.

Case B: The BN is used to provide the vehicle speed trajectory until the end of the trip.

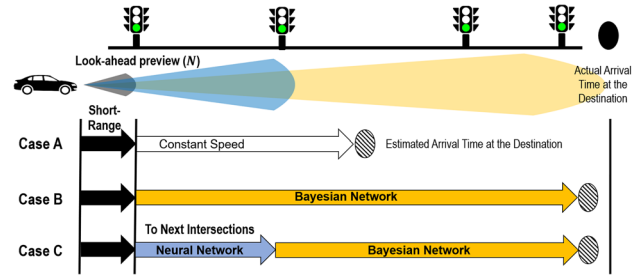


Fig. 12 The three cases (A–C) defined to evaluate the performance of MH-MPC with different types of information incorporated in the look-ahead

Case C: On the basis of case B, the vehicle speed preview in the medium-range is enhanced by the NN, while BN provides the vehicle speed prediction beyond the next intersection to the end of the trip.

Figure 12 illustrates the concepts of cases A–C. Note that in all three cases, the vehicle speed prediction over the short-range horizon (i.e., the receding horizon $N = 5$ s) is assumed to be accurate. For case A, the cruise speed in the long-range horizon varies at different segments of the corridor; specifically, it is around 15.6 m/s from intersections I–V and 20.8 m/s after intersection V. The trip end time is estimated based on the remaining distance and estimated vehicle speed profile, which will be updated each time when the estimated vehicle speed is updated.

Figure 12 shows how the predicted speeds over different ranges from Fig. 1 are combined for implementation in MH-MPC for iPTM. In case C, while the predicted speed over the medium-range is already available from the BN, the more accurate prediction obtained from the NN is used.

In order to analyze the performance of MH-MPC for three cases defined above, 140 vehicles are randomly selected among all the vehicles traveling through the entire corridor. The initial conditions, ambient temperature, and cabin heating demands are set to be the same for all the vehicles. The results of applying an offline dynamic programming (DP) are used as the benchmark [40] to show how the uncertainty and lack of information about the speed preview degrade the fuel consumption from its optimal value, thereby demonstrating how the proposed speed prediction framework helps to stay close to the global optimal solution. Figure 13 shows the probability density functions for fuel consumption increase of cases A–C as compared to DP solution. Note that for DP implementation, it is assumed that the entire vehicle speed is

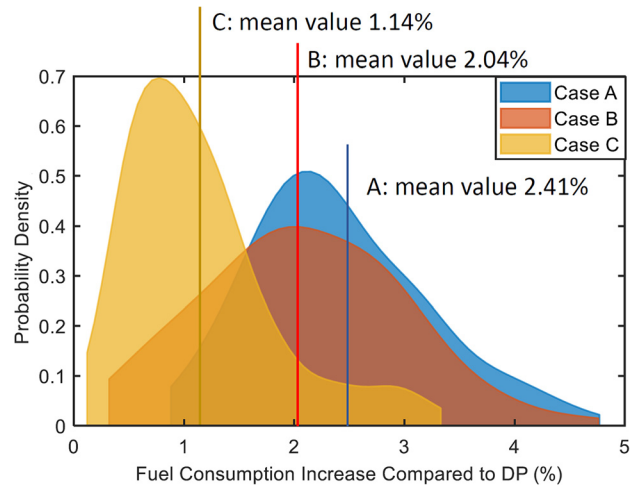


Fig. 13 The probability density function of the fuel consumption increase from cases A–C

known a priori with a sampling period of 1 s. To compute the probability densities in Fig. 13, we have used ksdensity function in MATLAB, which returns a kernel distribution through a nonparametric representation of the probability density function of a random variable [41]. In our case, the random variable is the fuel consumption increase percentage from the simulated vehicles as compared to the DP solution. The mean value of fuel consumption increase in case B is 2.04%, which is 0.37% lower than case A. It shows that by enhancing the vehicle speed prediction over the long shrinking horizon using the BN, the MH-MPC can improve fuel consumption.

The addition of medium-range speed prediction (case C) enhances the fuel consumption by 0.9% on average as compared to case B. In this case, 0.9% is nearly half the distance between case B and DP, meaning that case C provides significant incremental benefits of 50%, as compared to case B. Given the higher probability density of case C, as compared to case B, Fig. 13 suggests that an improved prediction of vehicle speed and passing/stopping events in the medium-range provides extra fuel savings. Overall, while a long prediction horizon is needed given the slow responding thermal dynamics of the system, further refining the speed prediction in the medium-range provides significant incremental benefits without the complexity of refining the entire long horizon.

In order to investigate the sensitivity of fuel consumption to the errors in the speed forecast, we consider two vehicles following two different branches of the BN (i.e., vehicle #1 from branch 5 and #2 from branch 3). Figure 14 shows the predicted vehicle speed profiles of these two vehicles before they approach intersection III. According to the BN, before intersection III, branch 5 has the highest probability for both vehicles. One can see that while the BN predicts all the passing/stopping events for vehicle #1 correctly, it mispredicts the event for vehicle #2 at intersection III ($t = 170$ s), see Fig. 14(b).

Figure 15 shows the fuel consumption of these two vehicles. It can be seen that, as compared to DP, the fuel consumption is larger in case A by 2.25% and 2.93% for vehicles #1 and #2, respectively. Additionally, as compared to case C, in case B the fuel consumption is increased by 0.51% and 0.90% for vehicles #1 and #2, respectively.

The state trajectories of two vehicles are shown in Figs. 16 and 17. It can be seen that the SOC and T_{cl} trajectories show a similar trend for all cases. At the beginning of the trip, when T_{cl} is not warm enough, i.e., around 50°C, the engine is used to meet the traction power demand and at the same time charge the battery.

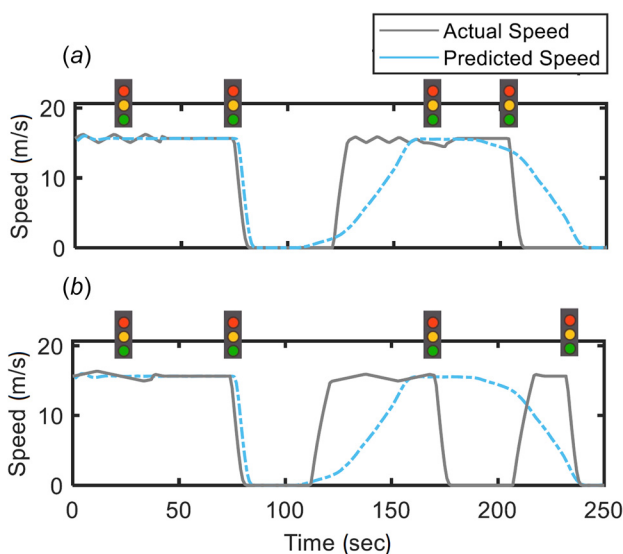


Fig. 14 The comparison of actual and predicted vehicle speed profiles before the vehicle approaches intersection III: (a) vehicle #1 and (b) vehicle #2

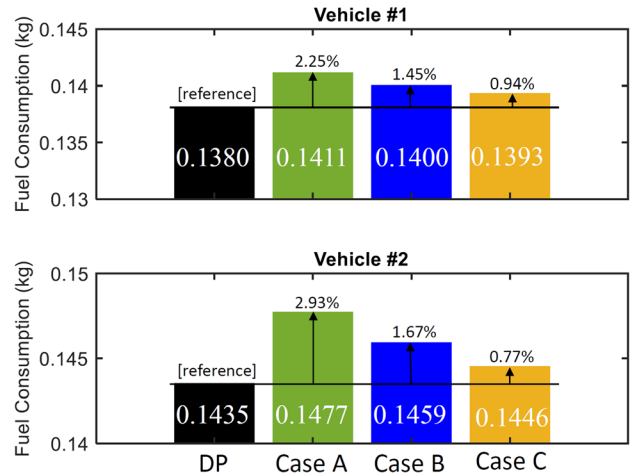


Fig. 15 Fuel consumption (kg) of DP, cases A-C

While SOC is pushed toward its upper limit, i.e., 80%, T_{cl} rises to around 60°C. Note that when the T_{cl} is lower than 60°C, the engine efficiency degrades significantly [37]. Therefore, by running the engine at a higher load, the controller is able to warm up the engine faster to enable fuel savings later during the drive. Note that, in order to fully recuperate the kinetic energy during braking, as shown in Figs. 16(b) and 17(b), the controller uses the battery to satisfy traction power demand prior to a stop/braking event. The subsequent reduction in SOC increases the amount of regenerative braking energy that can be recovered before reaching the maximum SOC constraint. Enabling this energy recovery requires the controller to accurately predict the upcoming stop/braking event. For case A, the controller cannot detect the stop event until the intersection is within the short receding horizon, leaving insufficient time for battery discharge. Therefore, the kinetic energy during the braking phases is not fully recuperated in case A. Moreover, for vehicle #2, the BN makes a

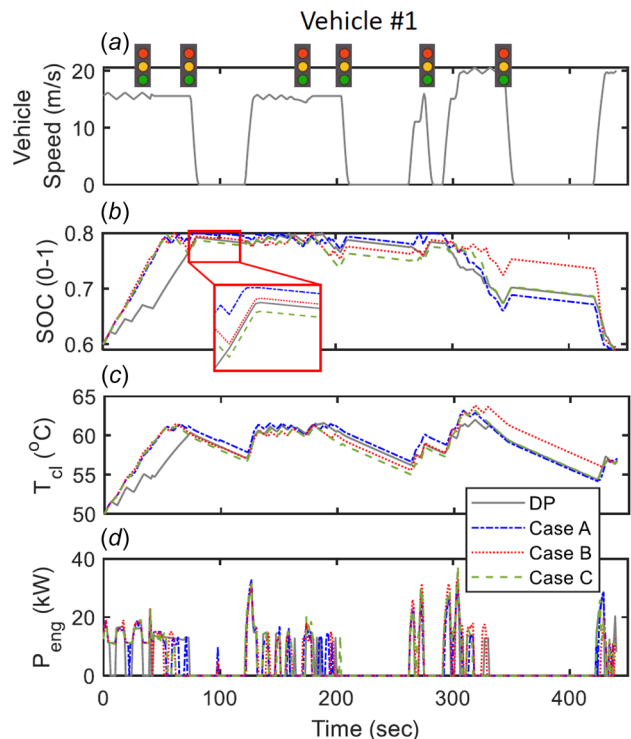


Fig. 16 State trajectories for vehicle #1: (a) vehicle speed, (b) battery SOC, (c) coolant temperature, and (d) engine power

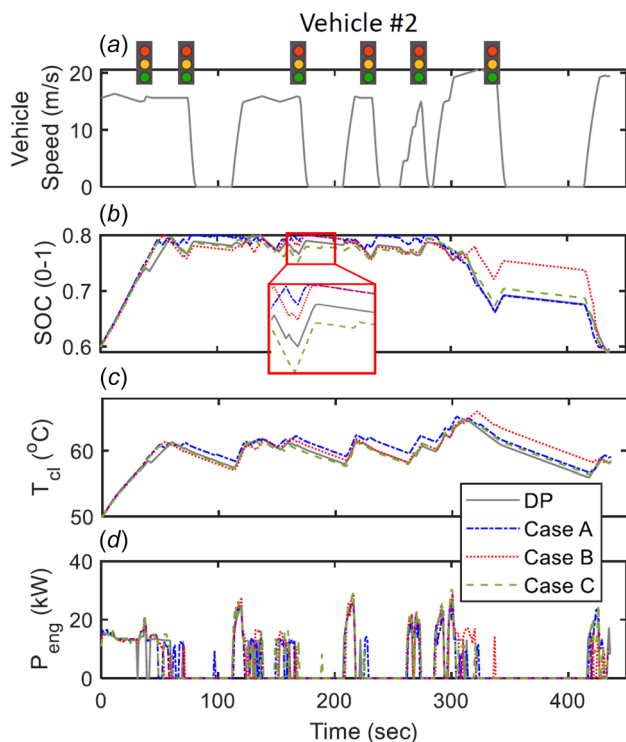


Fig. 17 State trajectories for vehicle #2: (a) vehicle speed, (b) battery SOC, (c) coolant temperature, and (d) engine power

misprediction at intersection III (around 170 s), and in case B, the stop is not detected in advance, and thus, the energy is not fully recuperated during braking.

6 Conclusion

In this paper, a novel data-driven multirange vehicle speed prediction strategy was proposed for urban corridors with signalized intersections. The proposed strategy exploits historical traffic data collected from connected vehicles to provide a prediction of vehicle speed over short-range, medium-range, and long-range. Over the short-range horizon, the vehicle speed prediction is obtained based on V2V/I communication, which is assumed of high accuracy. Over the long-range horizon, a BN provides the vehicle speed prediction and estimates the most probable driving scenario until the end of the trip. The medium-range prediction (from the end of the short-range to the next intersection) exploits a NN that is able to forecast the passing/stopping event at the next intersection with 90% accuracy based on the validation data. Then, the medium-range vehicle speed trajectory forecast is informed by exploiting the prediction of passing/stopping events and estimates of the queue length and stop/arrival time.

The effectiveness of the proposed vehicle speed prediction framework was demonstrated by exploiting it for vehicle speed preview in a MH-MPC scheme used for HEV IPTM. The MH-MPC exploits a short receding horizon and a longer shrinking horizon that extends to the end of the trip. The vehicle speed preview over the receding horizon is informed by V2V/V2I-based short-range vehicle speed prediction, while NN and BN-based approaches are used to inform the vehicle speed preview over the shrinking horizon. The simulation results show that by incorporating the medium- and long-range speed preview, the MH-MPC achieves a fuel consumption within a 1% deviation from the off-line dynamic programming solution. Furthermore, the sensitivity analysis revealed that by enhancing the accuracy of predicting the passing/stopping events, the performance of MH-MPC can be improved. Compared with constant vehicle speed preview, the

proposed multirange vehicle speed prediction reduces the fuel consumption by around 1.28%.

Potential future research directions include: (i) expanding the speed prediction framework to more complex scenarios where the signal timing policy is not fixed-time and may vary over time according to a specific policy, (ii) investigating the scalability of the BN-based driving scenario tree approach and distributed NN for longer corridors with a larger number of intersections, (iii) taking into account the variation in the driver behavior and aggressiveness level by adapting the long-term speed predictions with respect to individual vehicles' speeds in real-time, (iv) accounting for uncertainties associated with speed prediction over the short-range, and (v) assessing the robustness of the speed prediction and the IPTM to disturbances and uncertainties that are often hard to capture through historical traffic data, e.g., unscheduled stop or break.

Acknowledgment

Hao Wang and Connie Qiu from Ford Motor Company are gratefully acknowledged for their technical comments during the course of this study. Special thanks to Yiheng Feng and Zhen Yang from the University of Michigan for providing real-world traffic data.

Funding Data

- The University of Michigan portion of this work is funded in part by the U.S. Department of Energy (DOE), ARPA-E NEXTCAR program (Award No. DE-AR0000797; Funder ID: 10.13039/100000015).

Nomenclature

C_{bat}	= battery capacity (A h)
C_{eng}	= engine specific heat capacity (J/kg °C)
LHV	= lower heating value (J/kg)
M_{eng}	= equivalent thermal mass (kg)
\dot{m}_{fuel}	= fuel consumption rate (kg/s)
$\dot{m}_{\text{fuel,nom}}$	= nominal fuel consumption rate (kg/s)
P_{bat}	= battery power (W)
P_{eng}	= engine power (W)
P_{trac}	= traction power (W)
$P_{\text{aux}}^{\text{bat}}$	= battery power for auxiliary systems (W)
$P_{\text{trac}}^{\text{bat}}$	= battery power for traction (W)
Q_{air}	= heat rate rejected by air convection (W)
Q_{exh}	= heat rate rejected in the exhaust (W)
Q_{fuel}	= heat rate released in combustion process (W)
Q_{heat}	= heat rate exchanged for cabin heating (W)
R_{bat}	= battery resistance (Ω)
R_{int}	= battery internal resistance (Ω)
s_{bar}	= distance to stop bar (m)
s_{queue}	= queue length (m)
SOC	= battery state-of-charge
T_{arrival}	= arrival time (s)
T_{cl}	= engine coolant temperature (°C)
T_{dura}	= stop duration (s)
T_{queue}	= stop duration for queue discharge (s)
T_{signal}	= stop duration for signal switch (s)
T_{stop}	= stop time at next intersection (s)
U_{oc}	= battery open-circuit voltage (V)
Δt	= sampling time (s)

Acronyms

BN	= Bayesian network
CAV	= connected and automated vehicle
DP	= dynamic programming

HEV = hybrid electric vehicle
 iPTM = integrated power and thermal management
 MH-MPC = multihorizon model predictive control
 MPC = model predictive control
 NN = neural network
 V2V/I = vehicle-to-vehicle/infrastructure

References

- [1] Vahidi, A., and Sciarretta, A., 2018, "Energy Saving Potentials of Connected and Automated Vehicles," *Transp. Res. Part C: Emerging Technol.*, **95**, pp. 822–843.
- [2] Guanetti, J., Kim, Y., and Borrelli, F., 2018, "Control of Connected and Automated Vehicles: State of the Art and Future Challenges," *Annu. Rev. Control*, **45**, pp. 18–40.
- [3] Amini, M., Feng, Y., Yang, Z., Kolmanovsky, I., and Sun, J., 2020, "Long-Term Vehicle Speed Prediction Via Historical Traffic Data Analysis for Improved Energy Efficiency of Connected Electric Vehicles," *Transp. Res. Rec.*, **2674**(11), pp. 17–29.
- [4] Hu, Q., Amini, M., Feng, Y., Yang, Z., Wang, H., Kolmanovsky, I., Sun, J., Wiese, A., Qiu, Z., and Seeds, J. B., 2020, "Engine and Aftertreatment Co-Optimization of Connected HEVs Via Multi-Range Vehicle Speed Planning and Prediction," *SAE Technical Paper No. 2020-01-0590*.
- [5] Hu, Q., Amini, M., Wang, H., Kolmanovsky, I., and Sun, J., 2020, "Integrated Power and Thermal Management of Connected HEVs Via Multi-Horizon MPC," *ACC*, Denver, CO, pp. 3053–3058.
- [6] Panwai, S., and Dia, H., 2005, "Comparative Evaluation of Microscopic Car-Following Behavior," *IEEE Trans. Intell. Transp. Syst.*, **6**(3), pp. 314–325.
- [7] Lefèvre, S., Sun, C., Bajcsy, R., and Laugier, C., 2014, "Comparison of Parametric and Non-Parametric Approaches for Vehicle Speed Prediction," *American Control Conference*, Portland, OR, pp. 3494–3499.
- [8] Jing, J., Kurt, A., Ozatay, E., Michelini, J., Filev, D., and Ozguner, U., 2015, "Vehicle Speed Prediction in a Convoy Using V2V Communication," *International Conference on Intelligent Transportation Systems*, Las Palmas de Gran Canaria, Spain, pp. 2861–2868.
- [9] Platho, M., Groß, H.-M., and Eggert, J., 2013, "Predicting Velocity Profiles of Road Users at Intersections Using Configurations," *Intelligent Vehicles Symposium (IV)*, Gold Coast City, Australia, pp. 945–951.
- [10] Clark, S., 2003, "Traffic Prediction Using Multivariate Nonparametric Regression," *J. Transp. Eng.*, **129**(2), pp. 161–168.
- [11] Ma, X., Tao, Z., Wang, Y., Yu, H., and Wang, Y., 2015, "Long Short-Term Memory Neural Network for Traffic Speed Prediction Using Remote Microwave Sensor Data," *Transp. Res. Part C: Emerging Technol.*, **54**, pp. 187–197.
- [12] Fusco, G., Colombaroni, C., and Isaenko, N., 2016, "Short-Term Speed Predictions Exploiting Big Data on Large Urban Road Networks," *Transp. Res. Part C: Emerging Technol.*, **73**, pp. 183–201.
- [13] Jiang, X., and Adeli, H., 2005, "Dynamic Wavelet Neural Network Model for Traffic Flow Forecasting," *J. Transp. Eng.*, **131**(10), pp. 771–779.
- [14] Vanajakshi, L., and Rilett, L., 2004, "A Comparison of the Performance of Artificial Neural Networks and Support Vector Machines for the Prediction of Traffic Speed," *IEEE Intelligent Vehicles Symposium*, Parma, Italy, pp. 194–199.
- [15] Zhang, Y., and Xie, Y., 2007, "Forecasting of Short-Term Freeway Volume With V-Support Vector Machines," *Transp. Res. Rec.*, **2024**(1), pp. 92–99.
- [16] Park, J., Murphey, Y. L., McGee, R., Kristinsson, J., Kuang, M. L., and Phillips, A. M., 2014, "Intelligent Trip Modeling for the Prediction of an Origin–Destination Traveling Speed Profile," *IEEE Trans. Intell. Transp. Syst.*, **15**(3), pp. 1039–1053.
- [17] Jiang, B., and Fei, Y., 2017, "Vehicle Speed Prediction by Two-Level Data Driven Models in Vehicular Networks," *IEEE Trans. Intell. Transp. Syst.*, **18**(7), pp. 1793–1801.
- [18] Park, J., Murphey, Y. L., Kristinsson, J., McGee, R., Kuang, M., and Phillips, T., 2013, "Intelligent Speed Profile Prediction on Urban Traffic Networks With Machine Learning," *The 2013 International Joint Conference on Neural Networks (IJCNN)*, Dallas, TX, pp. 1–7.
- [19] Borhan, H., Zhang, C., Vahidi, A., Phillips, A., Kuang, M., and Di Cairano, S., 2010, "Nonlinear Model Predictive Control for Power-Split Hybrid Electric Vehicles," *49th CDC*, Atlanta, GA, pp. 4890–4895.
- [20] Di Cairano, S., Bernardini, D., Bemporad, A., and Kolmanovsky, I., 2014, "Stochastic MPC With Learning for Driver-Predictive Vehicle Control and Its Application to HEV Energy Management," *IEEE Trans. Control Syst. Technol.*, **22**(3), pp. 1018–1031.
- [21] Bichi, M., Ripaccioli, G., Di Cairano, S., Bernardini, D., Bemporad, A., and Kolmanovsky, I., 2010, "Stochastic Model Predictive Control With Driver Behavior Learning for Improved Powertrain Control," *49th CDC*, Atlanta, GA, pp. 6077–6082.
- [22] Borhan, H., Vahidi, A., Phillips, A., Kuang, M., Kolmanovsky, I., and Di Cairano, S., 2012, "MPC-Based Energy Management of a Power-Split Hybrid Electric Vehicle," *IEEE Trans. Control Syst. Technol.*, **20**(3), pp. 593–603.
- [23] Hemmati, S., Doshi, N., Hanover, D., Morgan, C., and Shahbakti, M., 2021, "Integrated Cabin Heating and Powertrain Thermal Energy Management for a Connected Hybrid Electric Vehicle," *Appl. Energy*, **283**, p. 116353.
- [24] PTV Group, 2016, "PTV Vissim 9.0 User Manual," PTV AG, Karlsruhe, Germany.
- [25] Yang, Z., Feng, Y., Gong, X., Zhao, D., and Sun, J., 2019, "Eco-Trajectory Planning With Consideration of Queue Along Congested Corridor for Hybrid Electric Vehicles," *Transp. Res. Rec.*, **2673**(9), pp. 277–286.
- [26] Amini, M., Gong, X., Wang, H., Feng, Y., Kolmanovsky, I., and Sun, J., 2019, "Sequential Optimization of Speed, Thermal Load, and Power Split in Connected HEVs," *ACC*, Philadelphia, PA, pp. 4614–4620.
- [27] Moser, D., Waschl, H., Schmied, R., Efindic, H., and Del Re, L., 2015, "Short Term Prediction of a Vehicle's Velocity Trajectory Using ITS," *SAE Int. J. Passenger Cars: Electron. Electr. Syst.*, **8**(2), pp. 364–370.
- [28] Zeng, T., Zhang, C., Hao, D., Cao, D., Chen, J., Chen, J., and Li, J., 2020, "Data-Driven Approach for Short-Term Power Demand Prediction of Fuel Cell Hybrid Vehicles," *Energy*, **208**, p. 118319.
- [29] Tang, X., Jia, T., Hu, X., Huang, Y., Deng, Z., and Pu, H., 2021, "Naturalistic Data-Driven Predictive Energy Management for Plug-In Hybrid Electric Vehicles," *IEEE Trans. Transp. Electr.*, **7**(2), pp. 497–508.
- [30] Zhang, F., Xi, J., and Langari, R., 2017, "Real-Time Energy Management Strategy Based on Velocity Forecasts Using V2V and V2I Communications," *IEEE Trans. Intell. Transp. Syst.*, **18**(2), pp. 416–430.
- [31] Sun, S., Zhang, C., and Yu, G., 2006, "A Bayesian Network Approach to Traffic Flow Forecasting," *IEEE Trans. Intell. Transp. Syst.*, **7**(1), pp. 124–132.
- [32] Jordan, M., 1998, *Learning in Graphical Models*, Springer, Dordrecht, The Netherlands.
- [33] Zidek, R., Kolmanovsky, I., and Bemporad, A., 2021, "Model Predictive Control for Drift Counteraction of Stochastic Constrained Linear Systems," *Automatica*, **123**, p. 109304.
- [34] Wang, P., Deng, H., Zhang, J., Wang, L., Zhang, M., and Li, Y., 2021, "Model Predictive Control for Connected Vehicle Platoon Under Switching Communication Topology," *IEEE Trans. Intell. Transp. Syst.*, pp. 1–14.
- [35] Gong, X., Wang, H., Amini, M., Kolmanovsky, I., and Sun, J., 2019, "Integrated Optimization of Power Split, Engine Thermal Management, and Cabin Heating for Hybrid Electric Vehicles," *Third CCTA*, Hong Kong, China, pp. 567–572.
- [36] Kim, N., and Rousseau, A., 2016, "Thermal Impact on the Control and the Efficiency of the 2010 Toyota Prius Hybrid Electric Vehicle," *Proc. Inst. Mech. Eng., Part D: J. Automob. Eng.*, **230**(1), pp. 82–92.
- [37] Kim, N., Rousseau, A., Lee, D., and Lohse-Busch, H., 2014, "Thermal Model Development and Validation for 2010 Toyota Prius," *SAE Technical Paper No. 2014-01-1784*.
- [38] Docimo, D. J., Kang, Z., James, K. A., and Alleyne, A. G., 2021, "Plant and Controller Optimization for Power and Energy Systems With Model Predictive Control," *ASME J. Dyn. Syst., Meas., Control*, **143**(8), p. 081009.
- [39] Hu, Q., Amini, M. R., Kolmanovsky, I., Sun, J., Wiese, A., and Seeds, J. B., 2021, "Multihorizon Model Predictive Control: An Application to Integrated Power and Thermal Management of Connected Hybrid Electric Vehicles," *IEEE Trans. Control Syst. Technol.* (in press).
- [40] Lodaya, D., Zeman, J., Okarmus, M., Mohon, S., Keller, P., Shutty, J., and Kondipati, N., 2020, "Optimization of Fuel Economy Using Optimal Controls on Regulatory and Real-World Driving Cycles," *SAE Int. J. Adv. Curr. Pract. Mobility*, **2**(3), pp. 1705–1716.
- [41] Hill, P., 1985, "Kernel Estimation of a Distribution Function," *Commun. Stat. - Theory Methods*, **14**(3), pp. 605–620.